IEEE Access
Multidisciplinary ⋮ Rapid Review ⋮ Open Access Journal

Received 9 May 2024, accepted 30 May 2024, date of publication 4 June 2024, date of current version 11 June 2024.

Digital Object Identifier 10.1109/ACCESS.2024.3409328

RESEARCH ARTICLE

Research on High-Precision Control of Hydraulic Excavator Based on Optimal Trajectory Planning

JUNXIANG CHEN, KELONG XU, XIANGDONG KONG, YUJIE GUO, AND CHAO AI

State Key Laboratory of Crane Technology, Yanshan University, Qinhuangdao 066004, China
Hebei Provincial Key Laboratory of Heavy Machinery Fluid Power Transmission and Control, Yanshan University, Qinhuangdao 066004, China

Corresponding author: Chao Ai (aichao@ysu.edu.cn)

This work was supported in part by the National Natural Science Foundation-Joint Fund under Grant U22A20178, and in part by the School Scientific Research Cultivation Project-Important Special Cultivation under Grant 2022BZZD001.

ABSTRACT In this article, the trajectory planning and high-precision motion control of an excavator based on the independent hydraulic system of the load port are studied. A trajectory planning algorithm based on the combination of a quintic non-uniform B-spline curve and improved sparrow algorithm and an oil inlet flow controller based on the time-varying secant barrier Lyapunov function (TSBLF) are designed. First, the traditional sparrow algorithm is innovatively improved in trajectory planning to make the generated trajectory time shorter, more stable and energy better. Then, the secant function and fixed time controller are first introduced in the design of the oil flow controller to ensure that the system error converges to the predefined boundary in finite time. At the same time, the RBF neural network is used to approximate the unmodeled error and disturbance of the system. Finally, the simulation verification is carried out with the common trenching conditions in the intelligent operation of the excavator. The results show that the generated trajectory has obvious advantages over the traditional sparrow algorithm. The trajectory tracking error can converge to the neighborhood near the equilibrium point in a fixed time while satisfying the constraints, and has high control accuracy.

INDEX TERMS Trajectory optimization, load port independence, neural network, barrier function, flow/pressure control.

I. INTRODUCTION

Excavators are the ''pearl'' product with the highest economic added value and the most abundant functions in engineering machinery. Excavators are widely used. With the updating and iterating of excavator design, they have gradually developed to become green, intelligent, and unmanned. As a result, excavators have necessary systematic intelligent operation abilities, including self-perception, self-planning, and self-execution, thus reducing the dependence on the driver's experience [1], [2], which creates higher requirements for the trajectory planning and motion control of the excavator. That is, while realizing the optimal trajectory planning of the bucket tooth tip of an excavator, it is also necessary to overcome the problems of low control accuracy, poor stability, and long times required to reach stable tracking due to factors such as high nonlinearity and unknown external disturbances in the excavator control system. This would allow the high-precision progressive tracking of the trajectory to be realized [3].

Trajectory planning is the basis of the intelligent operation of excavators. The planned path is related to the energy consumption, stability, and work efficiency of excavator operations. Polynomials are widely used to solve minimum time problems while maintaining the continuity of the trajectory motion. Wang et al. [4] selected an appropriate polynomial order as the optimal trajectory planning method by comparing different orders of polynomials for trajectory planning methods to plan the energy-optimized trajectory. Chu et al. [5] determined the continuous smooth trajectory of the end-effector of the robotic arm by a polynomial interpolation method. However, when the polynomial order becomes

The associate editor coordinating the review of this manuscript and approving it for publication was Tao Wang.

larger to pursue a higher-precision trajectory, it often leads to the generation of the Longe phenomenon and also makes the calculation more difficult.

The use of spline interpolation curves can effectively solve the above problems. Chen et al. [6] used a two-model optimization architecture to take into account the normalization parameters of the B-spline curve through an improved quintic B-spline interpolation model to generate a trajectory such that a robotic arm consumed less energy and was more stable. Huang et al. [7] used a quintic B-spline to interpolate the trajectory in the joint space and combined it with a genetic algorithm to obtain a time-impact integrated optimal trajectory planning method for a robotic arm. This type of method can well maintain the continuity of trajectory motion and allow various optimization algorithms to optimize the planning model. The main goal of trajectory optimization lies in the multi-objective optimization of energy, time, physical constraints, and motion continuity. Many scholars have adopted mainstream methods such as the particle swarm algorithm [8], [9], flocking algorithm [10], genetic algorithm [11], and ant colony algorithm [12], but they usually suffer from problems of local optimality, low search accuracy, complicated algorithms, and long computation times.

The sparrow algorithm [13], an optimization algorithm proposed in recent years, has the characteristics of high search accuracy, fast convergence speed, good stability, and strong robustness compared with other swarm intelligence optimization algorithms. Zhang et al. [14] proposed a highly smooth and time-saving trajectory planning method by introducing a tent chaotic map and an adaptive step factor to improve the sparrow algorithm. Huang et al. [15] proposed an improved sparrow search algorithm combining an elite strategy and a sine algorithm for the trajectory planning of an underwater flexible manipulator, which had a good nonlinear approximation ability.

The execution level of excavator intelligent assistance requires the control system to perform high-precision asymptotic tracking of the planned trajectory. In recent decades, the asymptotic tracking of the working trajectory of the excavator has received extensive attention. Due to the large tonnage of the excavator and the relatively heavy operation, there are widespread parameter uncertainties caused by the structural nonlinearity of the governing differential equations, the nonlinearity of the actuator friction, uncertainties of the structural parameters, such as the load, bulk modulus of the hydraulic oil, and viscous friction coefficient, as well as uncertain nonlinearities, such as external disturbances, oil leakage, and dynamic friction, which are difficult to model. Therefore, the modeling of the excavator's actuator is more complicated, and there are problems such as difficult parameter identification and large non-modeling errors. To improve the trajectory control accuracy of excavators, the widely used methods mainly include improved optimization algorithms to optimize the parameters of proportional–integral–derivative (PID) controllers [16], [17], adaptive robust control algorithms [18], [19], use of a synovial controller [20], and active disturbance rejection controller [21].

To improve the trajectory tracking accuracy of the excavator, Yang et al. [22] introduced a neural network to establish a dynamic surface asymptotic tracking controller, which could not only ensure the transient tracking performance of the system but also ensure the asymptotic stability of the system. Feng et al. [23] proposed an adaptive sliding mode control method based on a radial basis function (RBF) neural network to further improve the trajectory tracking accuracy of the excavator. In addition, to further improve the control accuracy and reduce energy consumption, the idea of an independent control of the load port has been proposed in recent years. Lyu et al. [24] proposed a new type of electro-hydraulic system combining independent metering valves and a variable pump, and they proposed the idea of a pump–valve combination, which had strong advantages in terms of tracking performance and energy consumption. Chen et al. [25] proposed an integrated double-loop motion control strategy for electro-hydraulic actuators to achieve accurate trajectory tracking of electro-hydraulic actuators under constraints.

The above control algorithms mainly focused on nonlinear compensation and steady-state tracking performance improvements and less on the transient performance of the control system. To limit the control error, the barrier Lyapunov function can effectively solve the above problems. Ilchmann et al. proposed the concept of transient control, designed a transient variable, and defined a Lyapunov function of the transient variable to design a controller to achieve system tracking control without violating the constraints [26]. Subsequently, Tee et al. directly designed a controller by constructing the obstacle Lyapunov function to realize the system tracking control, which could ensure that the system constraints were not violated [27].

In recent years, the controller of the barrier Lyapunov function (BLF) has received extensive attention from scholars. Dao and Ahn [28] used the combination of the barrier Lyapunov function (BLF) and the main controller based on the task coordinate frame (TCF) method in the control design, and they proposed an active disturbance rejection contour control scheme. Xu et al. [29] synthesized the prescribed performance function (PPF) and the barrier Lyapunov function (BLF). They proposed a novel backstepping controller for hydraulic systems to deal with the uncertainty of the system without violating the full state constraint and achieved the specified performance tracking.

In order to improve the problems of long trajectory planning time, high energy consumption, unstable motion and nonlinear dynamics and modeling uncertainty of hydraulic and mechanical systems during trajectory tracking in intelligent auxiliary operation of excavators. Different from previous studies, this paper innovatively improves the traditional sparrow algorithm in trajectory planning, and combines

it with the five-order non-uniform B-spline curve for trajectory planning. In order to track the planned trajectory, an oil inlet flow controller based on time-varying secant barrier Lyapunov function and RBF neural network is designed. Considering the energy efficiency of the system, the oil return pressure controller is designed to achieve high-precision and energy-efficient trajectory tracking control.

The main innovations of this article are as follows: (1) The improved sparrow algorithm population initialization adopted a cat map chaotic sequence to improve the randomness and global distribution ability of the initial population. Then, the individual was adjusted by Cauchy mutation and a tent chaotic disturbance to prevent the population from becoming too ''concentrated'' or ''dispersed.'' Finally, an adaptive explorer–follower quantity adjustment formula was introduced to balance the ability to find global and local optima, so that the planned trajectory was smoother and more stable, the time was shorter, and the energy was better. (2) The secant function and the fixed-time controller are innovatively introduced in the design process of the inlet flow controller to ensure that the system error converges to the predefined boundary in a limited time, and the dynamic characteristics of the system were better. At the same time, RBF neural network was used to approximate the unmodeled error and disturbance, so as to enhance the robust performance of the system and simplify the controller design. The transient tracking performance of the system was guaranteed, as was the asymptotic stability of the system.

The rest of this article is organized as follows. The physical model of the hydraulic excavator manipulator is established considering the unmodeled error and external disturbances in Section II. Section III introduces the trajectory planning method of a hydraulic excavator manipulator. Section IV introduces the construction method and stability analysis of the oil inlet flow controller and the oil return pressure controller. Section V presents the comparative simulation results of the mechanical arm of the hydraulic excavator. Section VI presents the conclusions of this paper.

II. PHYSICAL MODEL OF EXCAVATOR ARM

In this section, the excavator is modeled to provide preconditions for the controller design in Section IV.

The structure of the excavator studied in this paper is shown in Fig. 1, the driving cylinder is connected to the working device in a hinged form, and each joint is controlled by the cylinder to perform a composite motion so that the hydraulic excavator can complete the specified tasks. The trajectory planning of this paper does not consider the rotation of the rotary joint, but only considers the combined motion of the boom, stick, and bucket joint in a plane.

In this paper, the excavator manipulator shown in Fig. 1 is studied, and its dynamics equation is described as follows:

$$M(q)\ddot{q} + C(q,\dot{q})\dot{q} + B\dot{q} + G(q) + \Delta C(q,\dot{q})\dot{q} + \Delta B\dot{q} + \Delta G(q) = J_{ha}(q)(P_1A_1 - P_2A_2) + d_1 \quad (1)$$

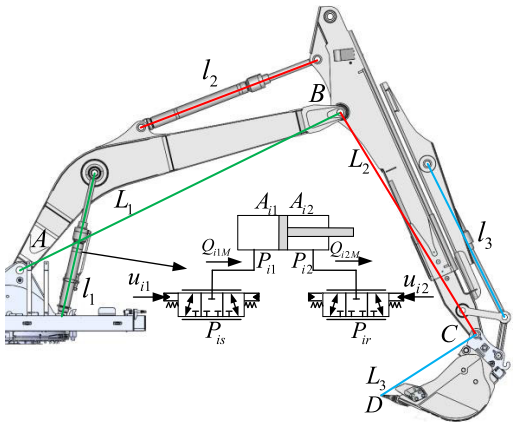

FIGURE 1. Hydraulic excavator.

where q, $\dot{q}$, and $\ddot{q}$ are the joint angle, velocity, and acceleration vectors, respectively, M represents the inertia matrix of the manipulator, C denotes the Coriolis force/centrifugal force matrix of the manipulator, G denotes the gravity vector matrix of the manipulator, B denotes the matrix of nodal viscous friction coefficients, $J_{ha}(q)(P_1A_1 - P_2A_2)$ denotes the vector of moments acting on the joints, where $J_{ha} = \partial x_{ha}/\partial q$, $x_{ha} = [x_{1ha}, x_{2ha}, x_{3ha}]^T$ denotes the displacement of the cylinder, d_1 denotes the total perturbation vector, and $\Delta C\dot{q}$, $\Delta B\dot{q}$, and ΔG denote the unmodeled parts of the coupled joint dynamics.

The pressures of the hydraulic cylinder rod cavity and the rodless cavity are, respectively

$$\begin{cases} \dot{P}_{i1} = \beta_e(-A_{i1}\dot{x}_{iha} - D_{i1} + Q_{i1})/V_{i1} + \Delta_{i1} \\ \dot{P}_{i2} = \beta_e(A_{i2}\dot{x}_{iha} + D_{i2} - Q_{i2})/V_{i2} + \Delta_{i2} \end{cases} \quad (2)$$

where β_e denotes the oil volume elastic modulus, $V_{i1} = V_{i01} + A_{i1}x_{iha}$ and $V_{i2} = V_{i02} - A_{i2}x_{iha}$ $(i = 1, 2, 3)$ are the volumes of the rodless and rodded cavities of the cylinder, respectively, V_{i01} and V_{i02} are the initial volumes of the rodless and rodded cavities of the cylinder, respectively, A_{i1} and A_{i2} are the piston areas of the rodless and rodded cavities of the cylinder, respectively, Q_{i1} and Q_{i2} are the inlet flow rate and the return flow rate, respectively, D_{i1} and D_{i2} are the un-modeled errors, and Δ_{i1} and Δ_{i2} are the unknown external perturbations.

Define $x_1 = q$, $x_2 = \dot{q}$, and $x_3 = P_1A_1 - P_2A_2$. The state space equations for the hydraulic excavator arm are established as follows:

$$\begin{aligned} \dot{x}_1 &= x_2 \; \dot{x}_2 = M^{-1}[J_{ha}x_3 - N_1 + N_2 + d_1] \\ \dot{x}_3 &= g_1Q_{1M} + g_2 - g_3x_2 - g_4 + d_2 \end{aligned} \quad (3)$$

in which

$$\begin{aligned} N_1 &= Cx_2 + Bx_2 + G \;\; N_2 = -\Delta M\dot{x}_2 - \Delta Cx_2 \\ &\quad - \Delta Bx_2 - \Delta G \\ d_2 &= A_1\Delta_1 - A_2\Delta_2 \;\; g_1 = A_1\beta_e/V \;\; g_2 = A_2\beta_eQ_{2M}/V_2 \\ g_3 &= \beta_eJ_{ha}\left(\frac{A_1^2}{V_1} + \frac{A_2^2}{V_2}\right) \;\; g_4 = \beta_e\left(\frac{A_1}{V_1} + \frac{A_2}{V_2}\right)(D_1 - D_2) \end{aligned} \quad (4)$$

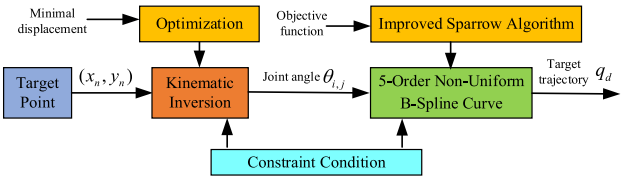

FIGURE 2. Trajectory planning process.

III. CONTROLLER DESIGN PROCEDURE

In this section, to address the problems of long trajectory times, high energy consumption, and unstable motion in the intelligent auxiliary operation planning of excavators, a trajectory planning algorithm combining the improved sparrow algorithm and a quintic non-uniform B-spline curve [30] is designed. The planning process is shown in Fig. 2.

The foraging process of the sparrow can be abstracted as a discoverer–joiner–alert model. The discoverer has the characteristics of high fitness and a wide search range to guide the population search and foraging. Participants follow the discoverer with the highest fitness for foraging. At the same time, to improve their predation rate, some participants will monitor the discoverers to compete for food or forage around them. When the alerter perceives a threat to the population surface, anti-predation behavior will be carried out. If the alarm value is greater than the safety threshold, the discoverer will take all the participants out of the dangerous area. The literature [31] is the traditional sparrow algorithm process. This paper improves the traditional sparrow algorithm based on the traditional sparrow algorithm.

To improve the randomness and ergodicity of the sparrow individual, the population is initialized by the cat map chaotic sequence and the reverse solution. The cat map is defined as

$$\begin{bmatrix} X_{s+1} \\ W_{s+1} \end{bmatrix} = \begin{bmatrix} 1 & a \\ b & ab+1 \end{bmatrix} \begin{bmatrix} X_s \\ W_s \end{bmatrix} \bmod \tag{5}$$

where a and b are arbitrary real numbers, and mod denotes the fractional part of the solution to a.

Randomly generate a feasible solution for the current population, denoted as:

$$\{X_s = [X_{s1}, X_{s2}, \cdots, X_{sd}, \cdots, X_{sD}]; X_{sd} \in [X_{\min}, X_{\max}]\} \tag{6}$$

Then, the reverse solution is

$$\begin{cases} X' = [X'_1, X'_2, \cdots X'_d, \cdots X'_D] \\ X'_{sd} = q(X_{\min} - X_{\max}) - X_{sd} \end{cases} \tag{7}$$

where q denotes a uniformly distributed real number in the interval [1, 0], and $X_{\min}$ and $X_{\max}$ are the boundaries of the feasible solutions.

To prevent the population from becoming too "concentrated" or "dispersed," the tent chaotic disturbance and Cauchy mutation are introduced to adjust the individual. At the same time, to avoid the characteristics of the tent map itself, prevent the population from falling into a small periodic point or an unstable periodic point, and not destroy the three characteristics of the chaotic variable, the random variable $rand(0, 1)/N_T$ is introduced to the original tent map expression. The tent mapping expression is:

$$z_{i+1} = \begin{cases} 2z_i + rand(0, 1)/N_T & 0 \le z \le \frac{1}{2} \\ 2(1 - z_i) + rand(0, 1)/N_T & \frac{1}{2} \le z \le 1 \end{cases} \tag{8}$$

The tent map is expressed by the Bernoulli shift transformation as follows:

$$z_{i+1} = (2z_i) \bmod + rand(0, 1)/N_T \tag{9}$$

where N_T denotes the number of particles within the chaotic sequence, and $rand(0, 1)$ is a random number in the range of [0, 1].

The chaotic variable Z_d is generated according to (9), and the chaotic variable Z_d is introduced into the solution space of the problem to be solved:

$$X^d_{new} = d_{\min} + (d_{\max} - d_{\min})Z_d \tag{10}$$

where $d_{\min}$ and $d_{\max}$ are the minimum and maximum values, respectively, of the dth dimensional variable X^d_{new}.

The chaotic perturbation of pairs of individuals is defined as follows:

$$X'_{new} = (X' + X_{new})/2 \tag{11}$$

where X' is the individual to be chaotically perturbed, X_{new} is the amount of chaotic perturbation generated, and X'_{new} is the individual after chaotic perturbation.

The Cauchy variant is

$$mutation(x) = x(1 + \tan(\pi(\tau - 0.5))) \tag{12}$$

where x denotes the original individual position, $mutation(x)$ denotes the individual position after Cauchy mutation, and τ denotes a random number in the interval of (0,1).

To improve the working efficiency of the hydraulic excavator and reduce energy consumption, it is generally expected that the hydraulic excavator should have the shortest movement time, the smoothest trajectory, and the least energy consumption. Therefore, the following optimization objective functions are defined:

$$F_1 = \sum_{i=1}^{n=1} h_i = T, i = 1, 2, \cdots, n-1$$
$$F_2 = \sum_{m=1}^{M} \sqrt{\frac{1}{T}\int_0^T \mathrm{a}_m^2 dt} \quad F_3 = \sum_{m=1}^{M} \sqrt{\frac{1}{T}\int_0^T \mathrm{j}_m^2 dt} \tag{13}$$

where h_i denotes the time of the robotic arm along each segment, n denotes the number of interpolation points, T denotes the total time of the robotic arm movement, a denotes the joint acceleration, j denotes the joint pulsation, F_1 denotes the movement time, which represents the efficiency of the robotic arm movement, F_2 denotes the average acceleration of the joint, which represents the energy consumption of the robotic arm, F_3 denotes the joint pulsation, which represents

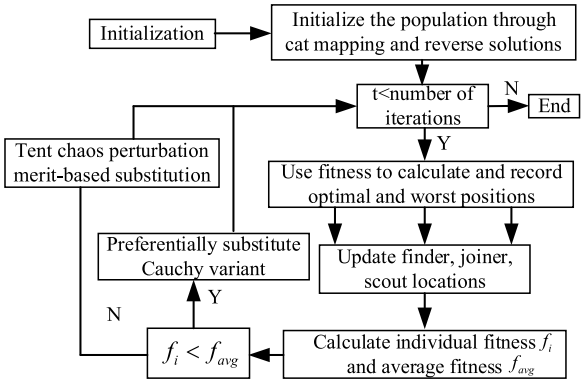

FIGURE 3. Improved sparrow algorithm process.

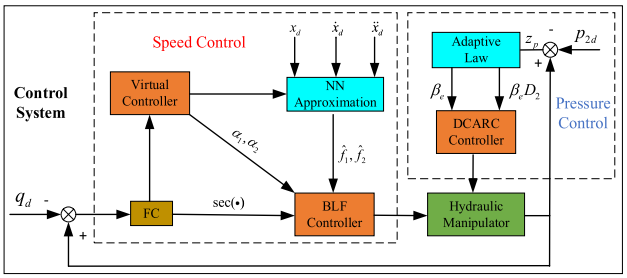

FIGURE 4. Load-port-independent system controller.

the smoothness of the trajectory, and M denotes the number of the key points of the trajectory.

The constraints are:

$$\left|\dot{\theta}\right| \leq V_{\max}, |a| \leq A_{\max}, |j| \leq R_{\max} \tag{14}$$

where $\dot{\theta}$, a, and j are the angular velocity, angular acceleration, and angular acceleration of the joint, respectively, and $V_{\max}$, $A_{\max}$, and $R_{\max}$ are the maximum angular velocity, maximum angular acceleration, and maximum angular acceleration allowed for the joint, respectively. The flowchart of the improved sparrow algorithm discussed in this subsection is shown in Fig. 3.

IV. LOAD-PORT-INDEPENDENT CONTROLLER DESIGN

Traditional hydraulic excavators often use proportional multi-way valves to control the actuator, resulting in pressure-flow coupling between the two chambers of the actuator. This approach cannot achieve separate throttling control and faces problems such as large energy consumption. The solution to this problem in this section is to use a load-port-independent system to control the pressure and flow of the two chambers of the actuator, and the trajectory tracking function of the cylinder is realized under the combined control of the flow and pressure. The control process is shown in Fig. 4.

A. OIL INLET FLOW CONTROLLER

In this section, an inlet flow controller based on a time-varying secant barrier Lyapunov function is designed, and the neural network is used to approximate the unmodeled

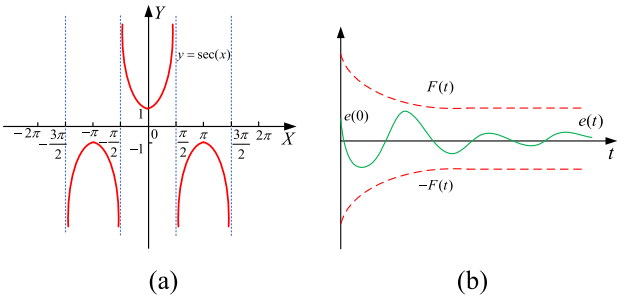

FIGURE 5. Functions: (a) secant function and (b) boundary function.

error and disturbance, so as to enhance the robust performance of the system and simplify the controller design.

The RBF neural network is composed of an input layer [32], hidden layer, and output layer. The transformation from the input layer to the hidden layer is nonlinear, the transformation from the hidden layer to the output layer is linear, and the neuron activation function of the hidden layer is an RBF. Any continuous unknown function $\Xi(X)$ can be approximated as

$$\Xi(X) = W^{*T}\phi(X) + \varepsilon \tag{15}$$

where $W^{*T} \in \mathbb{R}^{c\times v}$ denotes the weight vector, c and v are the number of outputs and the number of neurons in the hidden layer, respectively, $X \in \mathbb{R}^{z\times l}$ denotes the input to the neural network approximation error that satisfies $\|\varepsilon\| \leq \bar{\varepsilon}$, and $\bar{\varepsilon}$ is a positive constant. $\phi(X) = [\phi_1(X), \phi_2(X), \cdots, \phi_1(X)]$ is the excitation function, whose expression is

$$\phi_i(X) = \exp\left(-\frac{(X-\mu_i)^T(X_1-\mu_i)}{\sigma_i^2}\right), i = 1, 2, l \tag{16}$$

where μ_i and σ_i are the center and width of the Gaussian function of the ith neuron, respectively.

The following secant barrier Lyapunov function is selected:

$$V = \sec(\pi e/2F(t)) - 1 \tag{17}$$

where $\sec(\cdot)$ denotes the positive cut function, the image of which is shown in Fig. 5(a), $F(t)$ denotes the time-varying boundary with a function value greater than zero, and e denotes the system tracking error variable.

According to (17), when the error variable e crosses the time-varying boundary $\pm F(t)$, the value of the time-varying secant barrier Lyapunov function V will approach infinity. Therefore, as long as the controller is designed to ensure that V is bounded, it is possible to ensure that the system error e is always bounded within the time-varying boundary $(-F(t), F(t))$. Below, $\sec(\cdot)_i$ and $\tan(\cdot)_i$ are used to denote $\sec(\pi e_i/2F_i(t))$ and $\tan(\pi e_i/2F_i(t))$, $i = 1, 2, 3$, respectively. $F_i(t)$ is given by

$$F_i(t) = (F_{i0} - F_{i\infty})\exp^{-n_i t} + F_{i\infty} \tag{18}$$

where F_{i0}, $F_{i\infty}$, and n_i are all constants greater than zero and satisfy $0 < F_{i\infty} < F_{i0}$ and $\|e_1(0)\| < F_{i0}$. $e_1(0)$ represents the initial value of e_1. Its image is shown in Fig. 5(b).

Lemma 1:

$$\sec^{\gamma_1}(\cdot) > (\sec(\bullet)-1)^{\gamma_2} \quad \sec^{\gamma_2}(\cdot)-1 \geq (\sec(\cdot)-1)^{\gamma_2} \tag{19}$$

where γ_1 and γ_2 are constants greater than zero and satisfy $0 < \gamma_1 < 1$ and $\gamma_2 > 1$.

Lemma 2:

$$\lim_{x\to 0}\frac{\sec^{\gamma}(x)-1}{\tan(x)} = 0 \lim_{x\to 0}\frac{\partial\left(\sec^{\gamma}(x)-1\right)/\tan(x)}{\partial t} = \frac{\gamma}{2}\dot{x} \tag{20}$$

where γ is an arbitrary constant.

Lemma 3:

Let a continuous function $V(t)$ be positive definite and satisfy the following differential equation:

$$\dot{V}(t) \leq -\beta V + \xi \tag{21}$$

where $\beta > 0$ and $0 < \xi < 1$, at which point $V(t)$ satisfies the consistent eventual bounded convergence requirement.

Lemma 4 ([33]):

Suppose there exists a Lyapunov function $V(x)$ with constants $\alpha > 0, \beta > 0, 0 < \eta_0 < \infty, 0 < \gamma_1 < 1$, and $\gamma_2 > 1$ if the following equation holds:

$$\dot{V}(x) \leq -\alpha V(x)^{r_1} - \beta V(x)^{r_2} + \eta_0 \tag{22}$$

Then, $V(x)$ can converge in fixed time to a neighborhood near the equilibrium point, which can be expressed as

$$\left\{\lim_{t\to T} x \,\middle|\, V(x) \leq \min\left\{\left(\frac{\eta_0}{\alpha(1-\theta)}\right)^{r_1}, \left(\frac{\eta_0}{\beta(1-\theta)}\right)^{r_2}\right\}\right\} \tag{23}$$

where θ denotes a constant and satisfies the inequality $0 < \theta < 1$. The time required for the system variables to converge into the neighborhood satisfies the following inequality:

$$T \leq 1/\alpha\theta(1-r_1) + 1/\beta\theta(r_2-1) \tag{24}$$

The error variable e_1 and its derivative are, respectively, as follows:

$$e_1 = x_1 - x_{1d} \quad \dot{e}_1 = \dot{x}_1 - \dot{x}_{1d} = x_2 - \dot{x}_{1d} \tag{25}$$

The first Lyapunov function and its derivative are, respectively, as follows:

$$\begin{aligned} V_1 &= \sec(\pi e_1/2F_1(t)) - 1 \\ \dot{V}_1 &= \sec(\cdot)_1\tan(\cdot)_1((2\pi F_1\dot{e}_1 - 2\pi e_1\dot{F})/4F_1^2) \\ &= \pi\sec(\cdot)_1\tan(\cdot)_1(e_2+\alpha_1-\dot{x}_{1d}-\dot{F}e_1/F_1)/2F_1 \end{aligned} \tag{26}$$

where $e_2 = x_2 - \alpha_1$, and α_1 denotes the virtual control.

The virtual control law is designed according to (26) as follows:

$$\begin{aligned} \alpha_1 = \dot{x}_{1d} + \frac{\dot{F}_1}{F_1}e_1 - \frac{2F_1}{\pi\sec(\cdot)_1}\Big[\frac{k_{11}(\sec(\cdot)_1^{r_1}-1)}{\tan(\cdot)_1} \\ + \frac{k_{12}(\sec(\cdot)_1^{r_2}-1)}{\tan(\cdot)_1}\Big] \end{aligned} \tag{27}$$

where $\gamma_1, \gamma_2, k_{11}$, and k_{12} are constants greater than zero and satisfy $0 < \gamma_1 < 1$ and $\gamma_2 > 1$. It follows from Lemma 2 that there is no singular value problem for both α_1 and its derivatives, and substitution yields

$$\begin{aligned} \dot{V}_1 = -k_{11}(\sec(\cdot)_1^{r_1}-1) - k_{12}(\sec(\cdot)_1^{r_2}-1) \\ + \frac{\pi\sec(\cdot)_1\tan(\cdot)_1}{2F_1}e_2 \end{aligned} \tag{28}$$

According to (28), as long as e_2 is bounded and V_1 is uniformly and ultimately bounded, the first subsystem is stable. The boundedness of e_2 is proven below. The error variable and its derivative are, respectively, as follows:

$$\begin{aligned} e_2 = x_2 - \alpha_1 \quad \dot{e}_2 &= \dot{x}_2 - \dot{\alpha}_1 \\ &= M^{-1}\left[J_{ha}x_3 - N_1 + N_2 + d_1\right] - \dot{\alpha}_1 \end{aligned} \tag{29}$$

The second Lyapunov function and its derivative are, respectively, as follows:

$$\begin{aligned} V_2 &= V_1 + \sec(\cdot)_2 - 1 + \frac{1}{2\eta_{w_1}}\tilde{W}_1^T\tilde{W}_1 + \frac{1}{2\eta_{\varepsilon_1}}\tilde{\varepsilon}_1^T\tilde{\varepsilon}_1 \\ \dot{V}_2 &= \dot{V}_1 + \frac{\pi\sec(\cdot)_2\tan(\cdot)_2}{2F_2}(\dot{e}_2 - \frac{\dot{F}_2}{F_2}e_2) \\ &\quad - \frac{1}{\eta_{w_1}}\tilde{W}_1^T\dot{\hat{W}}_1 - \frac{1}{\eta_{\varepsilon_1}}\tilde{\varepsilon}_1^T\dot{\hat{\varepsilon}}_1 \\ &= -k_{11}(\sec(\cdot)_1^{r_1}-1) - k_{12}(\sec(\cdot)_1^{r_2}-1) \\ &\quad - \frac{1}{\eta_{w_1}}\tilde{W}_1^T\dot{\hat{W}}_1 - \frac{1}{\eta_{\varepsilon_1}}\tilde{\varepsilon}_1^T\dot{\hat{\varepsilon}}_1 \\ &\quad + \frac{\pi\sec(\cdot)_2\tan(\cdot)_2}{2F_2}[M^{-1}(J_{ha}e_3 + J_{ha}\alpha_2 - N_1) \\ &\quad + f_1 - \frac{\dot{F}_2}{F_2}e_2] \end{aligned} \tag{30}$$

where η_{m1} and η_{ε_1} are constants greater than zero, $\tilde{W}_1 = W_1^* - \hat{W}_1$, $\tilde{\varepsilon}_1 = \varepsilon_1^* - \hat{\varepsilon}_1$, $e_3 = x_3 - \alpha_2$, and $f_1 = M^{-1}(N_2 + d_1) - \dot{\alpha}_1 + \frac{F_2\sec(\cdot)_1\tan(\cdot)_1}{F_1\sec(\cdot)_2}\frac{e_2}{\tan(\cdot)_2}$.

The virtual control is designed according to (30) as follows:

$$\begin{aligned} \alpha_2 = {J_{ha}}^{-1}\left(-M\hat{f}_1 + N_1 + M\dot{F}e_2/F_2\right) \\ - \frac{2{J_{ha}}^{-1}MF_2}{\pi\sec(\cdot)_2}\left[\frac{k_{21}\left(\sec(\cdot)_2^{n_1}-1\right)}{\tan(\cdot)_2} + \frac{k_{22}\left(\sec(\cdot)_2^{r_2}-1\right)}{\tan(\cdot)_2}\right] \end{aligned} \tag{31}$$

Let $\hat{f}_1 = \hat{W}_1^T\phi(x_1) + \hat{\varepsilon}_1$, and substitute it into (30)

$$\begin{aligned} \dot{V}_2 = \sum_{i=1}^{2}\left[-k_{i1}(\sec(\cdot)_i^{r_1}-1) - k_{i2}(\sec(\cdot)_i^{r_2}-1)\right] \\ + \frac{\pi\sec(\cdot)_2\tan(\cdot)_2}{2F_2}[\tilde{W}_1^T\phi(x_1) + \tilde{\varepsilon}_1] - \frac{1}{\eta_{w_1}}\tilde{W}_1^T\dot{\hat{W}}_1 \\ + \frac{\pi\sec(\cdot)_2\tan(\cdot)_2}{2F_2}M^{-1}J_{ha}e_3 - \frac{1}{\eta_{\varepsilon_1}}\tilde{\varepsilon}_1^T\dot{\hat{\varepsilon}}_1 \end{aligned} \tag{32}$$

According to (32), the neural network weight update rate can be obtained as

$$\dot{\hat{W}}_1 = \eta_{w_1}\pi \sec(\cdot)_2 \tan(\cdot)_2 \phi(x_1)/2F_2 - \sigma_{w_1}\hat{W}_1 \tag{33}$$

$$\dot{\hat{\varepsilon}}_1 = \eta_{\varepsilon_1}\pi \sec(\cdot)_2 \tan(\cdot)_2/2F_2 - \sigma_{\varepsilon_1}\hat{\varepsilon}_1 \tag{34}$$

where σ_{w_1} and σ_{ε_1} are constants greater than zero. Substituting these into (32) yields

$$\begin{aligned}\dot{V}_2 = &\sum_{i=1}^{2}[-k_{i1}(\sec(\cdot)_i^{r_1} - 1) - k_{i2}(\sec(\cdot)_i^{r_2} - 1)] \\ &+ \frac{\sigma_{w_1}}{\eta_{w_1}}\tilde{W}_1^T\hat{W}_1 + \frac{\sigma_{\varepsilon_1}}{\eta_{\varepsilon_1}}\tilde{\varepsilon}_1^T\hat{\varepsilon}_1 + \frac{\pi \sec(\cdot)_2 \tan(\cdot)_2}{2F_2}M^{-1}J_{ha}e_3\end{aligned} \tag{35}$$

According to Young's inequality,

$$\begin{aligned}\tilde{W}_1^T\hat{W}_1 &= \tilde{W}_1^T\left(\hat{W}_1 - W_1^{*T} + W_1^{*T}\right) = -\tilde{W}_1^T\tilde{W}_1 + \tilde{W}_1^T W_1^{*T} \\ &\le -\tilde{W}_1^T\tilde{W}/2 + W_1^{*T}W_1^*/2\end{aligned} \tag{36}$$

Simplification of (35) yields

$$\begin{aligned}\dot{V}_2 \le &\sum_{i=1}^{2}[-k_{i1}\sec(\cdot)_i^{r_1} - k_{i2}\sec(\cdot)_i^{r_2}] \\ &- \sigma_{w_1}\tilde{W}_1^T\tilde{W}_1/2\eta_{w_1} - \sigma_{\varepsilon_1}\tilde{\varepsilon}_1^T\tilde{\varepsilon}_1/2\eta_{\varepsilon_1} \\ &+ \sigma_{w_1}W_1^{*T}W_1^*/2\eta_{w_1} \\ &+ \sigma_{\varepsilon_1}\varepsilon_1^{*T}\varepsilon_1/2\eta_{\varepsilon_1} + \pi \sec(\cdot)_2 \tan(\cdot)_2 M^{-1}J_{ha}e_3/2F_2\end{aligned} \tag{37}$$

It can be shown that V_2 is guaranteed to be uniformly bounded eventually as long as e_3 converges. The boundedness of e_3 is proven below. The error variables and their derivatives are defined as follows:

$$\begin{aligned}e_3 &= x_3 - \alpha_2 \\ \dot{e}_3 &= \dot{x}_3 - \dot{\alpha}_2 = g_1Q_{1M} + g_2 - g_3x_2 - g_4 + d_2 - \dot{\alpha}_2\end{aligned} \tag{38}$$

The third Lyapunov function and its derivative are, respectively, as follows:

$$\begin{aligned}V_3 &= V_2 + \sec(\cdot)_3 - 1 + \frac{1}{2\eta_{w_2}}\tilde{W}_2^T\tilde{W}_2 + \frac{1}{2\eta_{\varepsilon_2}}\tilde{\varepsilon}_2^T\tilde{\varepsilon}_2 \\ \dot{V}_3 &= \dot{V}_2 + \frac{\pi \sec(\cdot)_3 \tan(\cdot)_3}{2F_3}(\dot{e}_3 - \frac{\dot{F}_3}{F_3}e_3) \\ &\quad - \frac{1}{\eta_{w_2}}\tilde{W}_2^T\dot{\hat{W}}_2 - \frac{1}{\eta_{\varepsilon_2}}\tilde{\varepsilon}_2^T\dot{\hat{\varepsilon}}_2 \\ &\le \sum_{i=1}^{2}[-k_{i1}(\sec(\cdot)_i^{r_1} - 1) - k_{i2}(\sec(\cdot)_i^{r_2} - 1)] \\ &\quad - \frac{\sigma_{w_1}}{2\eta_{w_1}}\tilde{W}_1^T\tilde{W}_1 - \frac{\sigma_{\varepsilon_1}}{2\eta_{\varepsilon_1}}\tilde{\varepsilon}_1^T\tilde{\varepsilon}_1 \\ &\quad + \frac{\sigma_{w_1}}{2\eta_{w_1}}W_1^{*T}W_1^* + \frac{\sigma_{\varepsilon_1}}{2\eta_{\varepsilon_1}}\varepsilon_1^{*T}\varepsilon_1^* - \frac{1}{\eta_{w_2}}\tilde{W}_2^T\dot{\hat{W}}_2 \\ &\quad - \frac{1}{\eta_{\varepsilon_2}}\tilde{\varepsilon}_2^T\dot{\hat{\varepsilon}}_2 + \frac{\pi \sec(\cdot)_3 \tan(\cdot)_3}{2F_3}(g_1Q_{1M} + g_2 - g_3x_2 \\ &\quad + f_2 - \frac{\dot{F}_3}{F_3}e_3)\end{aligned} \tag{39}$$

where $f_2 = d_2 - g_4 - \dot{\alpha}_2 + \frac{F_3 \sec(\cdot)_2 \tan(\cdot)_2}{F_2 \sec(\cdot)_3 \tan(\cdot)_3}M^{-1}J_{ha}e_3$.

The inlet oil flow controller is designed according to (39) as follows:

$$\begin{aligned}Q_{1M} = g_1^{-1}[&-g_2 + g_3x_2 - \hat{f}_2 + \dot{F}e_3/F_3 \\ &- \frac{2F_3}{\pi \sec(\cdot)_3}(\frac{k_{31}(\sec(\cdot)_3^{r_1} - 1)}{\tan(\cdot)_3} + \frac{k_{32}(\sec(\cdot)_3^{r_2} - 1)}{\tan(\cdot)_3})]\end{aligned} \tag{40}$$

Substituting $\hat{f}_2 = \hat{W}_2^T\phi(x_2) + \hat{\varepsilon}_2$ yields

$$\begin{aligned}\dot{V}_3 \le &\sum_{i=1}^{3}[-k_{i1}(\sec(\cdot)_i^{r_1} - 1) - k_{i2}(\sec(\cdot)_i^{r_2} - 1)] \\ &- \frac{\sigma_{w_1}}{2\eta_{w_1}}\tilde{W}_1^T\tilde{W} - \frac{\sigma_{\varepsilon_1}}{2\eta_{\varepsilon_1}}\tilde{\varepsilon}_1^T\tilde{\varepsilon}_1 \\ &+ \frac{\sigma_{w_1}}{2\eta_{w_1}}W_1^{*T}W_1^* + \frac{\sigma_{\varepsilon_1}}{2\eta_{\varepsilon_1}}\varepsilon_1^{*T}\varepsilon_1^* - \frac{1}{\eta_{w_2}}\tilde{W}_2^T\dot{\hat{W}}_2 \\ &- \frac{1}{\eta_{\varepsilon_2}}\tilde{\varepsilon}_2^T\dot{\hat{\varepsilon}}_2 + \frac{\pi \sec(\cdot)_3 \tan(\cdot)_3}{2F_3}(\tilde{W}_2^T\phi(x_2) + \tilde{\varepsilon}_2)\end{aligned} \tag{41}$$

According to (41), the neural network weight update rates are obtained as follows:

$$\dot{\hat{W}}_2 = \eta_{w_2}\pi \sec(\cdot)_3 \tan(\cdot)_3 \phi(x_2)/2F_3 - \sigma_{w_2}\hat{W}_2 \tag{42}$$

$$\dot{\hat{\varepsilon}}_2 = \eta_{\varepsilon_2}\pi \sec(\cdot)_3 \tan(\cdot)_3/2F_3 - \sigma_{\varepsilon_2}\hat{\varepsilon}_2 \tag{43}$$

Substituting into (41) and simplifying it yields:

$$\begin{aligned}\dot{V}_3 \le &\sum_{i=1}^{3}[-k_{i1}(\sec(\cdot)_i^{r_1} - 1) - k_{i2}(\sec(\cdot)_i^{r_2} - 1)] \\ &- \sum_{j=1}^{2}(\frac{\sigma_{w_j}}{2\eta_{w_j}}\tilde{W}_j^T\tilde{W}_j + \frac{\sigma_{\varepsilon_j}}{2\eta_{\varepsilon_j}}\tilde{\varepsilon}_j^T\tilde{\varepsilon}_j) \\ &+ \sum_{j=1}^{2}(\frac{\sigma_{w_j}}{2\eta_{w_j}}W_j^{*T}W_j^* + \frac{\sigma_{\varepsilon_j}}{2\eta_{\varepsilon_j}}\varepsilon_j^{*T}\varepsilon_j^*)\end{aligned} \tag{44}$$

Since $\sec(\cdot)_i$ satisfies the inequality $\sec(\cdot)_2 \ge 1$, a further simplification of (44) yields the following:

$$\begin{aligned}\dot{V}_3 \le &-\sum_{i=1}^{3}k_{i2}(\sec(\cdot)_i - 1) - \sum_{j=1}^{2}(\frac{\sigma_{w_j}}{2\eta_{w_j}}\tilde{W}_j^T\tilde{W}_j + \frac{\sigma_{\varepsilon_j}}{2\eta_{\varepsilon_j}}\tilde{\varepsilon}_j^T\tilde{\varepsilon}_j) \\ &+ \sum_{j=1}^{2}(\sigma_{w_j}W_j^{*T}W_j^*/2\eta_{w_j} + \sigma_{\varepsilon_j}\varepsilon_j^{*T}\varepsilon_j^*/2\eta_{\varepsilon_j}) \\ \le &-\rho V_3 + \xi\end{aligned} \tag{45}$$

where $\rho = \min\{k_{12}, k_{22}, k_{32}, \sigma_{w1}, \sigma_{w2}, \sigma_{\varepsilon1}, \sigma_{\varepsilon2}\}$, and $\xi = \sum^{2}\left(\sigma_{w_j}W_j^{*T}W_j^*/2\eta_{w_j} + \sigma_s\varepsilon_j^{*T}\varepsilon_j^*/2\eta_{\varepsilon_j}\right)$.

By-Lemma 3, the two-sided integral satisfies

$$0 \le V_3 \le \mu(t) = \xi/\rho + [V_3(0) - \xi/\rho]\,e^{-\rho t} \tag{46}$$

When t tends to infinity, $0 \le V_3 \le \frac{\xi}{\rho}$. Because V_3 is bounded, it follows that the tracking error of the system is always bounded within the time-varying boundary $(-F_i(t), F_i(t))$.

Since V_3 is bounded, the error signals e_i, $\tilde{W}_j$, and $\tilde{\varepsilon}_j$ are bounded, i.e., there exist constants $\bar{W}_j$ and $\bar{\varepsilon}_j$ greater than zero that satisfy $\tilde{W}_j \leq \bar{W}_j$ and $\tilde{\varepsilon}_j \leq \bar{\varepsilon}_j$, respectively. Hence, the following inequality holds:

$$
\begin{aligned}
&-\left(\frac{\sigma_{w_j}}{2\eta_{w_j}}\dot{W}_j^T\dot{W}_j\right)^n-\left(\frac{\sigma_{\varepsilon_j}}{2\eta_{\varepsilon_j}}\bar{\varepsilon}_j^T\bar{\varepsilon}_j\right)^n\\
&\quad+\left(\frac{\sigma_{w_j}}{2\eta_{w_j}}\bar{W}_j^T\bar{W}_j\right)^n+\left(\frac{\sigma_{\varepsilon_j}}{2\eta_{\varepsilon_j}}\bar{\varepsilon}_j^T\bar{\varepsilon}_j\right)^n\geq 0\\
&-\left(\frac{\sigma_{w_j}}{2\eta_{w_j}}W_j^T\bar{W}_j\right)^n-\left(\frac{\sigma_{\varepsilon_j}}{2\eta_{\varepsilon_j}}\varepsilon_j^T\varepsilon_j\right)^{n_2}\\
&\quad+\left(\frac{\sigma_{w_j}}{2\eta_{w_j}}\pi_j^T\omega_j\right)^2+\left(\frac{\sigma_{\varepsilon_j}}{2\eta_{\varepsilon_j}}\varepsilon_j^T\varepsilon_j\right)^{n_2}\geq 0
\end{aligned}
\tag{47}
$$

Substituting (47) into (45) yields

$$
\begin{aligned}
\dot{V}_3\leq&\sum_{i=1}^{3}\left[-k_{i1}\left(\sec(\cdot)_i^n-1\right)-k_{i2}\left(\sec(\cdot)_i^{n_2}-1\right)\right]\\
&+\sum_{j=1}^{2}\left(\frac{\sigma_{w_j}}{2\eta_{w_j}}W_j^{*T}W_j^*+\frac{\sigma_{\varepsilon_j}}{2\eta_{\varepsilon_j}}\varepsilon_j^{*T}\varepsilon_j^*\right)\\
&-\sum_{j=1}^{2}\left(\left(\frac{\sigma_{w_j}}{2\eta_{w_j}}\bar{W}_j^{\tau}\dot{W}_j\right)^n+\left(\frac{\sigma_{\varepsilon_j}}{2\eta_{\varepsilon_j}}\bar{\varepsilon}_j^{\tau}\bar{\varepsilon}_j\right)^n\right)\\
&+\sum_{j=1}^{2}\left(\left(\frac{\sigma_{w_j}}{2\eta_{w_j}}\bar{W}_j^{\tau}\bar{W}_k\right)^n+\left(\frac{\sigma_{\varepsilon_j}}{2\eta_{\varepsilon_j}}\bar{\varepsilon}_j^{\tau}\bar{\varepsilon}_j\right)^n\right)\\
&+\sum_{j=1}^{2}\left(\left(\frac{\sigma_{w_j}}{2\eta_{w_j}}\bar{W}_j^T\bar{W}_j\right)^2+\left(\frac{\sigma_{\varepsilon_j}}{2\eta_{\varepsilon_j}}\bar{\varepsilon}_j^T\bar{\varepsilon}_j\right)^2\right)\\
&-\sum_{j=1}^{2}\left(\left(\frac{\sigma_{w_j}}{2\eta_{w_j}}\bar{W}_j^T\bar{W}_j\right)^n+\left(\frac{\sigma_{\varepsilon_j}}{2\eta_{\varepsilon_j}}\bar{\varepsilon}_j^T\bar{\varepsilon}_j\right)^n\right)
\end{aligned}
\tag{48}
$$

Because $0\leq\sec(\cdot)_i-1<\sec(\cdot)_i$, it can be determined that $\sec(\cdot)_i^{r_1}-1>(\sec(\cdot)_i-1)^{r_1}$ and $\sec(\cdot)_i^{r_2}-1>(\sec(\cdot)_i-1)^{r_2}$. In addition, (48) can be further simplified as

$$
\begin{aligned}
\dot{V}_3\leq&\sum_{i=1}^{3}\left[-k_{i1}\left(\sec()_i-1\right)^{r_i}-k_{ij}\left(\sec(\cdot)_i-1\right)^{r_2}\right]\\
&+\sum_{j=1}^{2}\left(\frac{\sigma_{w_j}}{2\eta_{w_j}}W_j^{*T}W_j^*+\frac{\sigma_{s_j}}{2\eta_{s_j}}\varepsilon_j^{*T}\varepsilon_j^*\right)+\vartheta\\
&-\sum_{j=1}^{2}\left(\left(\frac{\sigma_{w_j}}{2\eta_{w_j}}\bar{W}_j^{\tau}\tilde{W}_j\right)^{n_2}+\left(\frac{\sigma_{s_j}}{2\eta_{\varepsilon_j}}\bar{\varepsilon}_j^{\tau}\bar{\varepsilon}_j\right)^2\right)\\
&+\sum_{j=1}^{2}\left(\left(\frac{\sigma_{v_j}}{2\eta_{w_j}}\bar{W}_j^{\tau}\bar{W}_j\right)^{\tau_j}+\left(\frac{\sigma_{\varepsilon_j}}{2\eta_{s_j}}\bar{\varepsilon}_j^{r}\bar{\varepsilon}_j\right)^n\right)\\
&+\sum_{j=1}^{2}\left(\left(\frac{\sigma_{w_j}}{2\eta_{w_j}}\bar{W}_j^T\bar{W}_j\right)^n+\left(\frac{\sigma_{x_j}}{2\eta_{\varepsilon_j}}\bar{\varepsilon}_j^T\bar{\varepsilon}_j\right)^2\right)\\
&-\sum_{j=1}^{2}\left(\left(\frac{\sigma_{w_j}}{2\eta_{w_j}}\bar{W}_j^{\tau}\bar{W}_j\right)^n+\left(\frac{\sigma_{\varepsilon_j}}{2\eta_{\varepsilon_j}}\bar{\varepsilon}_j^T\bar{\varepsilon}_j\right)^n\right)
\end{aligned}
\tag{49}
$$

where $\vartheta=\sum_{i=1}^{3}k_{i1}$. The following can be obtained using Lemma 4:

$$
\dot{V}_3\leq-\alpha V_3^{r_1}-\beta V_3^{r_2}+\eta_0 \tag{50}
$$

where α, β, and η_0 are defined as follows:

$$
\begin{aligned}
\alpha&=\min\left\{k_{i1},\sigma_{wj}^{r_1},\sigma_{\varepsilon j}^{r_1}\right\}\\
\beta&=\min\left\{(2n)^{1-r_2}k_{i2},(2n)^{1-r_2}\sigma_{wj}^{r_2},(2n)^{1-r_2}\sigma_{\varepsilon j}^{r_2}\right\},\\
&\qquad i=1,2,3,j=1,2\\
\eta_0&=\sum_{j=1}^{2}\left(\left(\frac{\sigma_{w_j}}{2\eta_{w_j}}\bar{W}_j^T\bar{W}_j\right)^{r_1}+\left(\frac{\sigma_{\varepsilon_j}}{2\eta_{\varepsilon_j}}\bar{\varepsilon}_j^T\bar{\varepsilon}_j\right)^{r_1}\right.\\
&\quad\left.+\left(\frac{\sigma_{w_j}}{2\eta_{w_j}}\bar{W}_j^T\bar{W}_j\right)^{r_2}\right)\\
&\quad\times\sum_{j=1}^{2}\left(\left(\frac{\sigma_{\varepsilon_j}}{2\eta_{\varepsilon_j}}\bar{\varepsilon}_j^T\bar{\varepsilon}_j\right)^{r_2}+\frac{\sigma_{w_j}}{2\eta_{w_j}}W_j^{*T}W_j^*+\frac{\sigma_{\varepsilon_j}}{2\eta_{\varepsilon_j}}\varepsilon_j^{*T}\varepsilon_j^*\right)+\vartheta
\end{aligned}
\tag{51}
$$

Using Lemma 4, we can determine that V_3 converges in a neighborhood near the zero point at a fixed time T. The neighborhood expression is given by (23), and the convergence time expression is given by (24).

B. OIL RETURN PRESSURE CONTROLLER DESIGN

To determine the unique reference pressure of the two chambers under a given load force, the back pressure side is set at a lower constant pressure P_{2d} to keep the overall pressure at a lower level to save energy. According to [34] and [35], the return pressure control law is obtained as follows:

$$
\begin{aligned}
Q_{2M}&=Q_{2Ma}+Q_{2Ms}\ Q_{2Ma}=A_2\dot{x}_{ha}-\hat{\theta}_Q/\hat{\theta}_\beta\\
&\quad-V_2\dot{P}_{2d}\ /\hat{\theta}_\beta\\
Q_{2Ms}&=Q_{2Ms1}+Q_{2Ms2}\ Q_{2Ms1}=k_1V_{2z_p}/\theta_{\beta\min}\\
Q_{2Ms2}&=k_2V_{2z_p}/\theta_{\beta\min}
\end{aligned}
\tag{52}
$$

The adaptive law is

$$
\hat{\theta}_{p2}=\Pr oj_{\theta_{p2}}(\Gamma_p\tau_p) \tag{53}
$$

V. SIMULATION ANALYSIS

The trajectory planning mentioned above and the flow/pressure controller based on the load-port-independent hydraulic system were implemented in simulations, and the results are compared in this section to verify the feasibility and superiority of the theory described in this paper. The dynamics equation of the excavator manipulator was analyzed. The formulas of the inertia matrix M and gravity vector matrix G are as follows:

$$
\begin{aligned}
M&=\sum_{i=1}^{n}\left(m_iJ_v^{(i)T}J_v^{(i)}+I_iJ_w^{(i)T}J_w^{(i)}\right)\\
C_{ij}&=\frac{dM_{ij}}{dt}-\frac{1}{2}\sum_{k=1}^{n}\frac{\partial M_{jk}}{\partial\theta_i}\dot{\theta}_k\ G_i=\frac{\partial p}{\partial\theta_i}=\sum_{j=1}^{n}\frac{\partial p_j}{\partial\theta_i}
\end{aligned}
\tag{54}
$$

TABLE 1. Excavator manipulator-related parameters.

Parameter	Value	Parameter	Value
L_1	4.240 m	L_2	3.090 m
L_3	1.340 m	B_i	15Nm · s / rad
A_1	$8.6\times10^{-3}\,m^2$	A_2	$4.8\times10^{-3}\,m^2$
V_{01}	$1.29\times10^{-3}\,m^3$	V_{02}	$3.12\times10^{-3}\,m^3$
I_1	1336 kg · m^2	I_2	2052 kg · m^2
I_3	83 kg · m^2	m_1	762 kg
m_2	1621 kg	m_3	344 kg

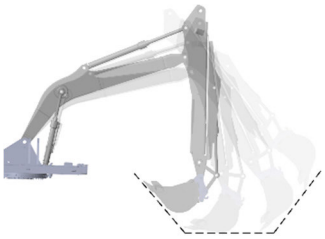

FIGURE 6. Excavator working conditions: trenching.

TABLE 2. Key points of trenching.

Trench end position (x, y, z, ξ)	Arm joint angle	Bucket rod joint angle	Bucket joint angle
(6.45,0,−0.80,−53.62)	28.75°	-71.84°	-10.53°
(6.10,0,-1.32,-68.30)	25.87°	-74.45°	-19.72°
(5.55,0,-1.72,-86.85)	24.01°	-79.05°	-31.81°
(5.00,0,-1.90,-103.07)	23.38°	-84.35°	-42.00°
(4.45,0,-1.90,-121.87)	22.79°	-88.86°	-55.8°
(3.90,0,-1.72,-133.95)	24.67°	-96.76°	-61.86°
(3.35,0,-1.32,-53.39)	26.48°	-104.25°	-78.44°
(3.00,0,-0.80,-174.05)	29.62°	-110.49°	-93.18°

where m_i denotes the mass of each rod, I_i denotes the rotational inertia of each rod, and $J_v^{(i)}$ and $J_w^{(i)}$ denote the velocity and angular velocity Jacobi matrices of each rod, respectively. The inertia matrix M, the Coriolis force/centrifugal force matrix C, and the gravity vector matrix C, are defined as follows:

$$M = \begin{bmatrix} M_{11} & M_{12} & M_{13} \\ M_{21} & M_{22} & M_{23} \\ M_{31} & M_{32} & M_{33} \end{bmatrix}, C = \begin{bmatrix} C_{11} & C_{12} & C_{13} \\ C_{21} & C_{22} & C_{23} \\ C_{31} & C_{32} & C_{33} \end{bmatrix}, \quad G = \begin{bmatrix} G_1 \\ G_2 \\ G_3 \end{bmatrix} \tag{55}$$

The relevant parameter data are shown in Table 1.

A. TRAJECTORY PLANNING SIMULATION ANALYSIS

This section simulates the trenching of the auxiliary working conditions commonly used in excavators, as shown in Fig. 6. After setting the key points of TABLE 2 the trajectory for the trenching target, the optimal joint angles of each joint

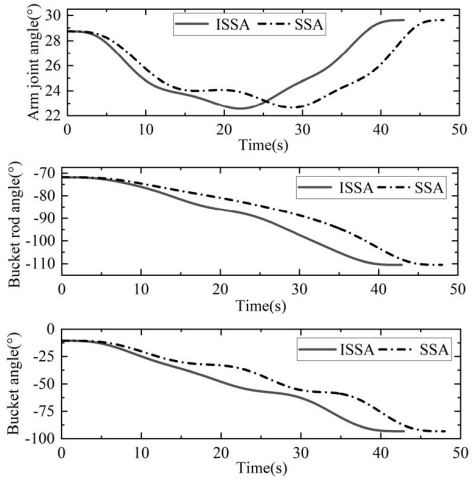

FIGURE 7. Ditching condition angle optimization.

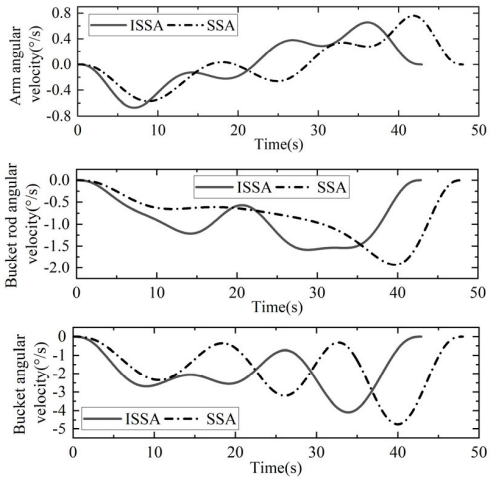

FIGURE 8. Optimization of angular velocity under trenching conditions.

at the key points were optimized and inversely solved for. Then, the trajectory was planned by a five-order non-uniform B-spline and the improved sparrow algorithm. In this section, the proposed trajectory planning method is compared with the trajectories planned using a quintic non-uniform B-spline but not optimized by the algorithm and optimized using the unimproved sparrow algorithm to verify the superiority of the trajectory planning algorithm proposed in this paper.

The sparrow population in the improved sparrow algorithm was set to 200, the number of iterations was 50, the proportion of discoverers was 20%, the proportion of early warnings was 20%, and the mutation probability was 35%.

The key points for trenching and slope repair are shown in Table 2. The trajectories planned by both the ISSA and the SSA satisfied the requirement that the angular velocity and angular acceleration were 0 at the beginning and end of the trajectory. According to Fig. 7, the trajectory time generated by the improved sparrow algorithm was reduced by 9.1% compared with that of the sparrow algorithm. According to Fig. 8, with the ISSA, the amplitude of the moving arm was reduced by 0.8%, the amplitude of the bucket rod was reduced

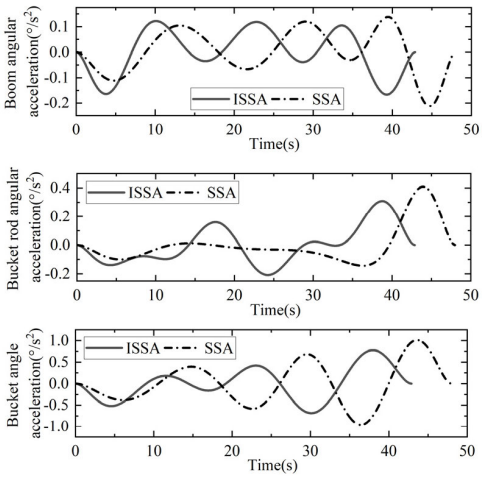

FIGURE 9. Optimization of angular velocity under trenching conditions.

by 17.9%, and the amplitude of the bucket was reduced by 13.1% compared with the those obtained by the SSA optimization, which indicates that the trajectory optimized by the improved sparrow algorithm could reduce energy consumption of the excavator and make it more energy efficient. According to Fig. 9, the amplitude of the moving arm was reduced by 17.5%, the amplitude of the bucket bar was reduced by 8%, and the amplitude of the bucket was reduced by 25.2%, which indicated that the trajectory optimized by the improved sparrow algorithm had lower pulsations, and the planned trajectory was more stable. The highest peak value of the improved sparrow algorithm was lower than that of the sparrow algorithm, and the trajectory fluctuations were smoother, which would make the service life of the excavator longer, more stable, and more efficient. To summarize, the trajectories generated using the improved sparrow algorithm were significantly shorter and smoother and had lower energy than the trajectories generated by the sparrow algorithm. This proved that the trajectory planning algorithm proposed in this paper has significant superiority over the trajectory planning by the traditional sparrow algorithm.

B. SIMULATION ANALYSIS OF TRAJECTORY ASYMPTOTIC TRACKING

The purpose of this section is to verify the tracking effect of the inlet oil flow controller and the return oil pressure controller designed in this paper for the planned trajectory and to compare the results with those of the sliding mode controller and a controller based on the traditional time-varying obstacle Lyapunov function. The trajectory to be tracked in this section was given in the trajectory planning section. To verify the accuracy of the neural network's estimation of the unmodeled error of the system, the unmodeled error of the system was set to be 5% of the standard value of the model, that is:

$$N_{i2} = -0.05M\dot{x}_2 - 0.05C_i x_2 - 0.05B_i x_2 - 0.05G_i$$
$$D_{i1} = 0.05A_{i1}\dot{x}_{iha} - 0.05Q_{i1}\ D_{i2} = 0.05A_{i2}\dot{x}_{iha} - 0.05Q_{i2} \tag{56}$$

The perturbations were set to

$$\begin{cases} d_{11} = 2 \times 10^4 \sin t\ N \cdot m \\ d_{12} = 4 \times 10^3 \sin t\ N \cdot m \\ d_{13} = 4 \times 10^2 \sin t\ N \cdot m \end{cases}$$
$$\begin{cases} d_{2i} = 1 \times 10^5 \sin t\ Pa \cdot m^2/s \\ d_{2i} = 2 \times 10^4 \sin t\ Pa \cdot m^2/s \\ d_{2i} = 1 \times 10^4 \sin t\ Pa \cdot m^2/s \end{cases} \tag{57}$$

The innovation of this paper mainly lies in the design o the oil flow controller in the control system. Therefore, this section mainly compares the oil flow controller in the contro system with different controllers to verify the superiority o the controller in this paper. The unmodeled error of the system model was set to 5% of its nominal value, and the relevant parameters of the oil pressure controller were designed as follows: $k_1 = 30, k_2 = 12, \omega_p = \text{diag}(1.2, 3)$ and $\Gamma_p = \text{diag}\left(1 \times 10^{-8}, 2.2 \times 10^{-3}\right)$.

The results are compared with the following three controllers:

1) Sliding mode control (SMC) [36]: The controller is a direct adaptive neural network control for a class of strictly feedback affine nonlinear systems with unknown nonlinearity. The virtual controller is designed as

$$\begin{aligned} \alpha_1 &= -k_1 e_1 - \hat{W}_1^T \phi(X_1)\ \alpha_2 \\ &= -e_1 - k_2 e_2 - \hat{W}_2^T \phi(X_2) \end{aligned} \tag{58}$$

The controller output is defined as

$$u = -e_2 - k_3 e_3 - \hat{W}_3^T \phi(X_3) \tag{59}$$

The adaptive law is

$$\dot{\hat{W}}_i = \eta_{wi} e_i \phi(X_i) - \sigma_{wi} \hat{W}_i,\ i = 1, 2, 3, 4 \tag{60}$$

2) Time logarithm barrier Lyapunov function (TLBLF) [37]: A controller based on the traditional time-varying barrier Lyapunov function with a virtual controller design is designed as follows:

$$\begin{aligned} \alpha_1 &= \dot{x}_d + \dot{k}_{a1} e_1 / k_{a1} - k_1 e_1 \\ \alpha_2 &= J_{ha}(M\hat{f}_1 + N_1 + M\dot{k}_{a2} e_2 / k_{a2} - M(k_{a2}^2 \\ &\quad - e_2^T e_2) e_1 / (k_{a1}^2 - e_1^T e_1) - M k_2 e_2) \end{aligned} \tag{61}$$

The controller output is defined as

$$\begin{aligned} u = g_1^{-1}(\hat{f}_2 + g_3 x_2 + \frac{\dot{k}_{a3}}{k_{a3}} e_3 \\ - \frac{e_2^T J_{ha}(k_{a3}^2 - e_3^T e_3)}{M(k_{a2}^2 - e_2^T e_2)} - k_3 e_3) \end{aligned} \tag{62}$$

The adaptive law is

$$\begin{aligned} \dot{\hat{W}}_i &= -\eta_{wi} e_{i+1}^T \phi(X_i) / (k_{ai+1}^2 - e_{i+1}^T e_{i+1}) - \sigma_{wi} \hat{W}_i \\ \dot{\hat{\varepsilon}}_i &= -\eta_{\varepsilon i} e_{i+1}^T / (k_{ai+1}^2 - e_{i+1}^T e_{i+1}) - \sigma_{\varepsilon i} \hat{\varepsilon}_i \end{aligned} \tag{63}$$

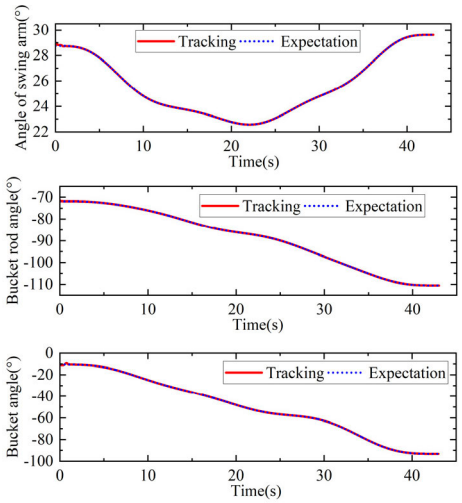

FIGURE 10. Track following.

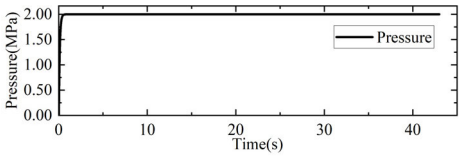

FIGURE 11. Back pressure.

3) Time secant barrier Lyapunov function (TSBLF): This was the controller designed in this paper, and the initial positions of the system were $x_{10} = 29°$, $x_{20} = -71.6°$, and $x_{30} = -11°$. The relevant parameter values of the controller were $k_{11} = k_{21} = k_{31} = 9$, $k_{12} = k_{22} = k_{32} = 11$, $r_{11} = r_{21} = r_{31} = 0.8$, and $r_{12} = r_{22} = r_{32} = 2$. The number of nodes in the hidden layer of the RBF neural network was set to 32, and the initial values of the neural network weights were $W_{1i0} = W_{2i0} = 0.2$, $i = 1, 2, \ldots, 32$. Furthermore, $\varepsilon_{10} = \varepsilon_{20} = 0$, $\eta_{w_1} = \eta_{w_2} = 1$, $\eta_{\varepsilon_1} = \eta_{\varepsilon_2} = 200$, $\sigma_{w_1} = \sigma_{w_2} = 0.15$, $\sigma_{\varepsilon_1} = \sigma_{\varepsilon_2} = 0.12$, and the interval of the center value was [−1.5,1.5]. The boundary functions were set as follows: $F_1 = 0.1e^{-0.8t} + 0.01$, $F_2 = 0.8e^{-t} + 0.1$, and $F_3 = 1.2e^{-0.8t} + 1.1$.

The tracking effect of the controller proposed in this paper on the boom and bucket is shown in Fig. 10. Fig. 11 shows the pressure controlled by the oil return pressure controller, which showed that the steady-state system pressure was maintained at 2 MPa, and thus the controller could effectively realize the energy saving effect. The tracking errors of each joint angle of the three controllers are shown in Fig. 12. According to Fig.12, the error dynamic responses of different controllers was analyzed. It could be clearly seen that the error dynamic responses of TSBLF and TLBLF controllers were better, and the error dynamic response of SMC controller was the worst. Compared with the TLBLF controller, the error overshoot of the TSBLF controller in the boom, stick and bucket were reduced by 28.6 %, 93.8 % and 85.7 %, respectively, and the time to reach stability were reduced by

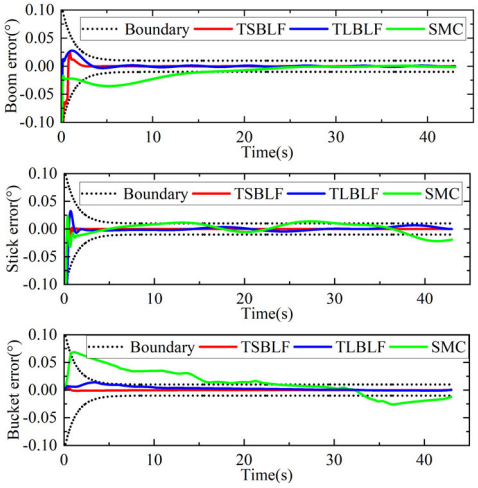

FIGURE 12. Angle tracking error of each joint.

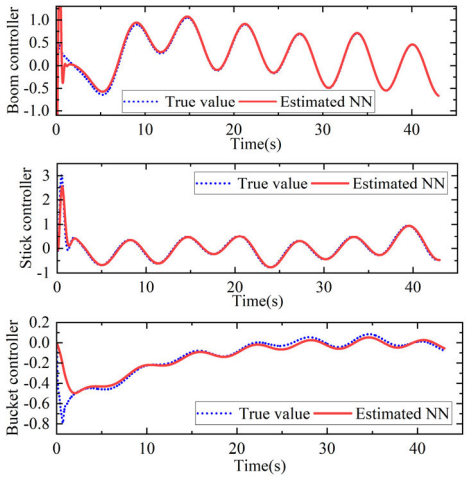

FIGURE 13. Estimation of each joint controller f1.

28.3 %, 39.4 % and 85.5 %, respectively. This was due to the introduction of a fixed time controller in the TSBLF controller, and the error dynamic characteristics were better than the TLBLF controller. The tracking accuracy of different controllers was analyzed. Because the neural network was used to approximate the unmodeled error and disturbance of the system, the robustness of the system was enhanced, and the three controllers had high control accuracy. Under the condition that the parameters of the neural network were set the same, both TSBLF and TLBLF controllers could constrain the error under the prescribed boundary. In the transient phase, the mean values of the error extremums of TSBLF and TLBLF controllers (the mean values of the difference between the maximum and minimum values in the error curves of the boom, the stick and the bucket) were 0.01 mm and 0.026 mm, respectively. In the steady-state phase, they were 0.001 mm and 0.01 mm, respectively. This is because the secant function and the logarithmic function ensured that the system state constraints were not violated. The mean value of the error extremum of the SMC controller in the transient phase was

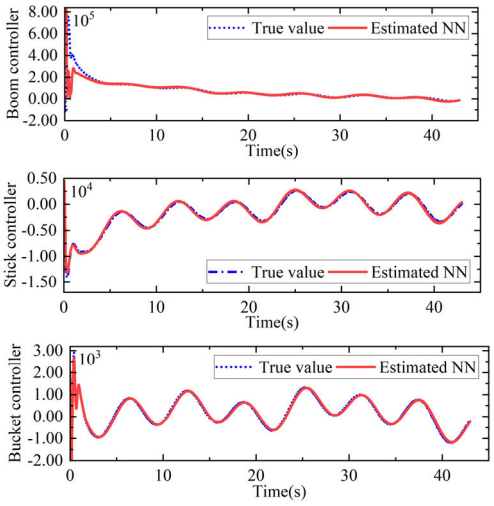

FIGURE 14. Estimation of each joint controller f2.

0.06 mm, and the steady-state phase was 0.04 mm. This was due to the lacked of error constraint function, resulted in the error of the SMC controller crossed the preset boundary. In summary, the TSBLF controller proposed in this paper had higher control accuracy and could also make the system error converge to the predefined boundary in a finite time, and had better error dynamic response. The neural network estimation proposed in the paper is shown in Figs. 13 and 14, where it can be seen that its estimation error for real modeling was small and the fit was high.

VI. CONCLUSION

In this paper, a control algorithm for optimal trajectory planning and high-precision tracking of hydraulic manipulator of excavator bucket tip is proposed. Firstly, a trajectory planning algorithm based on the combination of quintic non-uniform B-spline curve and improved sparrow algorithm is designed to solve the problems of long planning trajectory time, high energy consumption and unstable motion. The innovation point is that the improved sparrow algorithm introduces cat mapping, Cauchy mutation and Tent chaotic disturbance. By improving the group initialization ability and the optimization ability in the solution process, the planned trajectory is smoother and more stable, the time is shorter and the energy is better. Then, in order to make the excavator track the planned trajectory, the oil flow controller is designed based on the time-varying secant barrier Lyapunov function and RBF neural network, and it is applied to the load port independent system for the first time. The innovation is that the secant function and the fixed-time controller are introduced into the barrier Lyapunov controller, so that the system tracking error can converge to the neighborhood near the equilibrium point in a fixed time while satisfying the constraints. Finally, the stability is proved. The designed controller can not only ensure the transient tracking performance of the system, but also ensure the asymptotic stability of the system.

The research in this paper shows that the improved sparrow algorithm proposed in this paper has obvious advantages over the traditional sparrow algorithm. The introduction of secant function and fixed time controller makes the design of obstacle Lyapunov controller more possible, which can provide more theoretical basis for the research of excavator auxiliary intelligence. The deficiency of this paper is that the existence of obstacles is not considered in this paper. The future research plan is to improve the optimization algorithm and controller, and apply it to the actual excavator operation for verification.

REFERENCES

[1] J. Mattila, J. Koivumäki, D. G. Caldwell, and C. Semini, "A survey on control of hydraulic robotic manipulators with projection to future trends," *IEEE/ASME Trans. Mechatronics*, vol. 22, no. 2, pp. 669–680, Apr. 2017.

[2] J. Koivumäki and J. Mattila, "Stability-guaranteed impedance control of hydraulic robotic manipulators," *IEEE/ASME Trans. Mechatronics*, vol. 22, no. 2, pp. 601–612, Apr. 2017.

[3] M. Ramezani and S. Tafazoli, "Using artificial intelligence in mining excavators: Automating routine operational decisions," *IEEE Ind. Electron. Mag.*, vol. 15, no. 1, pp. 6–11, Mar. 2021.

[4] X. Wang, W. Sun, E. Li, and X. Song, "Energy-minimum optimization of the intelligent excavating process for large cable shovel through trajectory planning," *Structural Multidisciplinary Optim.*, vol. 58, no. 5, pp. 2219–2237, May 2018.

[5] X. Chu, Q. Hu, and J. Zhang, "Path planning and collision avoidance for a multi-arm space maneuverable robot," *IEEE Trans. Aerosp. Electron. Syst.*, vol. 54, no. 1, pp. 217–232, Feb. 2018.

[6] W. Chen, H. Wang, Z. Liu, and K. Jiang, "Time-energy-jerk optimal trajectory planning for high-speed parallel manipulator based on quantum-behaved particle swarm optimization algorithm and quintic B-spline," *Eng. Appl. Artif. Intell.*, vol. 126, Nov. 2023, Art. no. 107223.

[7] J. Huang, P. Hu, K. Wu, and M. Zeng, "Optimal time-jerk trajectory planning for industrial robots," *Mechanism Mach. Theory*, vol. 121, pp. 530–544, Mar. 2018.

[8] Z. Yao, S. Zhao, X. Tan, W. Wei, and Y. Wang, "Real-time task-oriented continuous digging trajectory planning for excavator arms," *Autom. Construct.*, vol. 152, Aug. 2023, Art. no. 104916.

[9] Ö. Ekrem and B. Aksoy, "Trajectory planning for a 6-axis robotic arm with particle swarm optimization algorithm," *Eng. Appl. Artif. Intell.*, vol. 122, Jun. 2023, Art. no. 106099.

[10] Y. Li, Y. Lu, D. Li, M. Zhou, C. Xu, X. Gao, and Y. Liu, "Trajectory optimization of high-speed robotic positioning with suppressed motion jerk via improved chicken swarm algorithm," *Appl. Sci.*, vol. 13, no. 7, p. 4439, Mar. 2023.

[11] A. Seddaoui and C. M. Saaj, "Collision-free optimal trajectory generation for a space robot using genetic algorithm," *Acta Astronautica*, vol. 179, pp. 311–321, Feb. 2021.

[12] F. Z. Baghli, L. E. Bakkali, and Y. Lakhal, "Optimization of arm manipulator trajectory planning in the presence of obstacles by ant colony algorithm," *Proc. Eng.*, vol. 181, pp. 560–567, Jun. 2017.

[13] J. Xue and B. Shen, "A novel swarm intelligence optimization approach: Sparrow search algorithm," *Syst. Sci. Control Eng.*, vol. 8, no. 1, pp. 22–34, Jan. 2020.

[14] X. Zhang, F. Xiao, X. L. Tong, J. Yun, Y. Liu, Y. Sun, B. Tao, J. Kong, M. Xu, and B. Chen, "Time optimal trajectory planning based on improved sparrow search algorithm," *Frontiers Bioeng. Biotechnol*, vol. 10, p. 852408, Mar. 2022.

[15] H. Huang, G. Tang, H. Chen, J. Wang, L. Han, and D. Xie, "Vibration suppression trajectory planning of underwater flexible manipulators based on incremental kriging-assisted optimization algorithm," *J. Mar. Sci. Eng.*, vol. 11, no. 5, p. 938, Apr. 2023.

[16] H. Feng, C. Yin, W. Ma, H. Yu, and D. Cao, "Parameters identification and trajectory control for a hydraulic system," *ISA Trans.*, vol. 92, pp. 228–240, Sep. 2019.

[17] H. Feng, C.-B. Yin, W.-W. Weng, W. Ma, J.-J. Zhou, W.-H. Jia, and Z.-L. Zhang, "Robotic excavator trajectory control using an improved GA based PID controller," *Mech. Syst. Signal Process.*, vol. 105, pp. 153–168, May 2018.

[18] L. Lyu, Z. Chen, and B. Yao, "High precision and high efficiency control of pump and valves combined hydraulic system," in *Proc. IEEE 15th Int. Workshop Adv. Motion Control (AMC)*, Mar. 2018, pp. 391–396.

[19] B. Yao and S. Liu, "Energy-saving control of hydraulic systems with novel programmable valves," in *Proc. 4th World Congr. Intell. Control Autom.*, 2002, pp. 322–3219.

[20] H. Feng, J. Jiang, X. Chang, C. Yin, D. Cao, H. Yu, C. Li, and J. Xie, "Adaptive sliding mode controller based on fuzzy rules for a typical excavator electro-hydraulic position control system," *Eng. Appl. Artif. Intell.*, vol. 126, Nov. 2023, Art. no. 107008.

[21] Z. Gao, D. Zhang, S. Zhu, and J.-E. Feng, "Distributed active disturbance rejection control for Ackermann steering of a four-in-wheel motor drive vehicle with deception attacks on controller area networks," *Inf. Sci.*, vol. 540, pp. 370–389, Nov. 2020.

[22] X. Yang, W. Deng, and J. Yao, "Neural adaptive dynamic surface asymptotic tracking control of hydraulic manipulators with guaranteed transient performance," *IEEE Trans. Neural Netw. Learn. Syst.*, vol. 34, no. 10, pp. 1–11, Oct. 2022.

[23] H. Feng, Q. Song, S. Ma, W. Ma, C. Yin, D. Cao, and H. Yu, "A new adaptive sliding mode controller based on the RBF neural network for an electro-hydraulic servo system," *ISA Trans.*, vol. 129, pp. 472–484, Oct. 2022.

[24] L. Lyu, Z. Chen, and B. Yao, "Development of pump and valves combined hydraulic system for both high tracking precision and high energy efficiency," *IEEE Trans. Ind. Electron.*, vol. 66, no. 9, pp. 7189–7198, Sep. 2019.

[25] Z. Chen, B. Helian, Y. Zhou, and M. Geimer, "An integrated trajectory planning and motion control strategy of a variable rotational speed pump-controlled electro-hydraulic actuator," *IEEE/ASME Trans. Mechatronics*, vol. 28, no. 1, pp. 588–597, Feb. 2023.

[26] A. Ilchmann, E. P. Ryan, and S. Trenn, "Tracking control: Performance funnels and prescribed transient behaviour," *Syst. Control Lett.*, vol. 54, no. 7, pp. 655–670, Jul. 2005.

[27] K. P. Tee, S. S. Ge, and E. H. Tay, "Barrier Lyapunov functions for the control of output-constrained nonlinear systems," *Automatica*, vol. 45, no. 4, pp. 918–927, Apr. 2009.

[28] H. V. Dao and K. K. Ahn, "Active disturbance rejection contouring control of robotic excavators with output constraints and sliding mode observer," *Appl. Sci.*, vol. 12, no. 15, p. 7453, Jul. 2022.

[29] Z. Xu, W. Deng, H. Shen, and J. Yao, "Extended-state-observer-based adaptive prescribed performance control for hydraulic systems with full-state constraints," *IEEE/ASME Trans. Mechatronics*, vol. 27, no. 6, pp. 5615–5625, Dec. 2022.

[30] Z. Chen, X. Xu, W. Zha, A. Rodic, and P. B. Petrovic, "Motion planning of 7-DOF manipulator based on quintic B-spline curve," in *Proc. 6th IEEE Int. Conf. Adv. Robot. Mechatronics (ICARM)*, Chongqing, China, Jul. 2021, pp. 858–862.

[31] S. Yan, W. Liu, X. Li, P. Yang, F. Wu, and Z. Yan, "Comparative study and improvement analysis of sparrow search algorithm," *Wireless Commun. Mobile Comput.*, vol. 2022, pp. 1–15, Aug. 2022.

[32] B. Chen, H. Zhang, and C. Lin, "Observer-based adaptive neural network control for nonlinear systems in nonstrict-feedback form," *IEEE Trans. Neural Netw. Learn. Syst.*, vol. 27, no. 1, pp. 89–98, Jan. 2016.

[33] J. Gao, Z. Fu, and S. Zhang, "Adaptive fixed-time attitude tracking control for rigid spacecraft with actuator faults," *IEEE Trans. Ind. Electron.*, vol. 66, no. 9, pp. 7141–7149, Sep. 2019.

[34] B. Yao, "Desired compensation adaptive robust control," *J. Dyn. Syst., Meas., Control*, vol. 131, no. 6, Nov. 2009, Art. no. 061001.

[35] B. Yao, F. Bu, J. Reedy, and G. T.-C. Chiu, "Adaptive robust motion control of single-rod hydraulic actuators: Theory and experiments," *IEEE/ASME Trans. Mechatronics*, vol. 5, no. 1, pp. 79–91, Mar. 2000.

[36] S. S. Ge and C. Wang, "Direct adaptive NN control of a class of nonlinear systems," *IEEE Trans. Neural Netw.*, vol. 13, no. 1, pp. 214–221, Jan. 2002.

[37] L. Ding, S. Li, Y.-J. Liu, H. Gao, C. Chen, and Z. Deng, "Adaptive neural network-based tracking control for full-state constrained wheeled mobile robotic system," *IEEE Trans. Syst. Man, Cybern. Syst.*, vol. 47, no. 8, pp. 2410–2419, Aug. 2017.

JUNXIANG CHEN was born in Henan, China, in 1996. He received the master's degree in mechanical engineering from Yanshan University, Qinhuangdao, China, in 2021, where he is currently pursuing the Ph.D. degree in mechanical engineering.

His research interests include the optimization design of hydraulic and control systems for construction machinery.

KELONG XU was born in Handan, Hebei, China, in 2000. He received the B.S. degree in mechanical engineering and automation from Yanshan University, Qinhuangdao, China, in 2022, where he is currently pursuing the master's degree.

His main research interests include the optimization design of hydraulic and control systems for construction machinery.

XIANGDONG KONG was born in Qiqihar, Heilongjiang, China, in 1959. He received the B.S. degree in mechanical engineering from Zhejiang University, Hangzhou, China, in 1982, the M.S. degree in fluid power transmission and control from the Northeast Heavy Machinery College, Qiqihar, in 1985, and the Ph.D. degree in fluid power transmission and control from Yanshan University, Qinhuangdao, China, in 1991.

Since 1991, he has been with Yanshan University, where he was a Lecturer and an Associate Professor, from 1991 to 1994. From 1994 to 1996, he was the Deputy Director of the Department of Mechanical and Electrical Control Engineering, Yanshan University. From 1996 to 1997, he was the Director of the President Office, Yanshan University. Since 1996, he has been a Professor with Yanshan University, where he was the Dean of the School of Mechanical Engineering, from 1997 to 2003. Since 2003, he has been the Vice President and the Ph.D. Supervisor with Yanshan University. His current research interests include fluid power transmission and control, intelligent hydraulic wind power, fluid vibration and suppression, electro-hydraulic servo systems, the optimum design of hydraulic components, and the theory and control of conveyor turbines.

YUJIE GUO was born in Handan, Hebei, China, in 2000. He received the B.S. degree in mechanical engineering and automation from Yanshan University, Qinhuangdao, China, in 2022, where he is currently pursuing the master's degree.

His main research interests include the optimization design of hydraulic and control systems for construction machinery.

CHAO AI was born in Tangshan, Hebei, China, in 1982. He is currently a Professor/a Ph.D. Supervisor. He has long been committed to the research of high-performance control of intelligent hydraulic components and systems. He has presided more than ten sub-projects of the National Key Research and Development Program, the National Natural Science Foundation of China, and provincial and ministerial projects. He has published more than 70 academic articles, including 28 in SCI/EI and three books. He is a Young Scholar of the "Changjiang Scholars Award Program" of the Ministry of Education, an excellent young and young top-notch talent in Hebei province, the Deputy Director of the Intelligent Flow Control Branch of the Mechanical Engineering Society, and an Evaluation Expert of high-tech enterprises in Hebei province.